Journal of Zhejiang University-SCIENCE A (Applied Physics & Engineering) *2024 25(5):429-442*
www.jzus.zju.edu.cn; www.springer.com/journal/11582
E-mail: jzus_a@zju.edu.cn

Research Article
https://doi.org/10.1631/jzus.A2300339

Comparative analysis between single-train passing and double-train intersection in a tunnel

Jianming DU[1], Qian FANG[2]✉, Xuan ZHANG[1], Hualao WANG[1]

[1]*Bridge and Tunnel Research Center, Research Institute of Highway Ministry of Transport, Beijing 100088, China*
[2]*Tunnel and Underground Engineering Research Center of Ministry of Education, Beijing Jiaotong University, Beijing 100044, China*

Abstract: Aerodynamic pressure significantly impacts the scientific evaluation of tunnel service performance. The aerodynamic pressure of two trains running in a double-track tunnel is considerably more complicated than that of a single train. We used the numerical method to investigate the difference in aerodynamic pressure between a single train and two trains running in a double-track tunnel. First, the numerical method was verified by comparing the results of numerical simulation and on-site monitoring. Then, the characteristics of aerodynamic pressure were studied. Finally, the influence of various train–tunnel factors on the characteristics of aerodynamic pressure was investigated. The results show that the aerodynamic pressure variation can be divided into stage I: irregular pressure fluctuations before the train tail leaves the tunnel exit, and stage II: periodic pressure declines after the train tail leaves the tunnel exit. In addition, the aerodynamic pressure simultaneously jumps positively or drops negatively for a single train or two trains running in double-track tunnel scenarios. The pressure amplitude in the two-train case is higher than that for a single train. The maximum positive peak pressure difference (P_{STP}) and maximum negative peak pressure difference (P_{STN}) increase as train speed rises to the power from 2.256 to 2.930 in stage I. The P_{STP} and P_{STN} first increase and then decrease with the increase of tunnel length in stage I. The P_{STP} and P_{STN} increase as the blockage ratio rises to the power from 2.032 to 2.798 in stages I and II.

Key words: Railway tunnel; Aerodynamic effect; Pressure characteristic; Train speed; Tunnel length; Blockage ratio

1 Introduction

Pressure waves caused by a train travelling through a tunnel at high speed are continuously reflected and superimposed between the tunnel entrance and exit, resulting in a series of aerodynamic pressures (Howe, 2007; Rivero et al., 2018; Saito and Fukuda, 2020). Under continuous aerodynamic pressure effects, the initial defects inside tunnel structures (such as voids and cracks) tend to further initiate, expand, and even penetrate, causing lining-structure incompletion, bearing-capability reduction, and shortening of tunnel service life (Gong and Zhu, 2018; Liu et al., 2019b; Du et al., 2021, 2022b). Therefore, aerodynamic pressure research is significant for railway tunnels.

✉ Qian FANG, qfang@bjtu.edu.cn
Jianming DU, https://orcid.org/0000-0002-1850-8991
Qian FANG, https://orcid.org/0000-0002-8148-9228

Received July 1, 2023; Revision accepted Oct. 15, 2023;
Crosschecked Mar. 28, 2024; Online first May 15, 2024

In this study, we systematically studied the characteristics of aerodynamic pressure associated with train–tunnel factors, using theoretical analysis, a numerical method, on-site monitoring, and laboratory tests. The relevant factors included the speed and formation type of trains, the length and entrance hood of the tunnel, and the blockage ratio. For the case of a single train travelling through a tunnel, the characteristics of aerodynamic pressure associated with train speed and formation, as well as tunnel length, have been previously analyzed through field monitoring (Ko et al., 2012; Chen ZW et al., 2017; Liu et al., 2019b). The influence of train speed and nose length, and the tunnel entrance hood, on tunnel aerodynamic pressure has been studied numerically (Chen XD et al., 2017; Zhang et al., 2017; Du et al., 2022c). Within this context, a series of laboratory tests was used to investigate the characteristics of aerodynamic pressure associated with train speed and formation, and the tunnel portal (Yang et al., 2016; Du et al., 2020). The effects of the tunnel entrance hood and hood geometry on tunnel aerodynamic

pressure have also been explored using theoretical analysis (Howe, 2007; Howe et al., 2008; Saito, 2019). For the case of two trains intersecting in a double-track tunnel, the influence of train speed and tunnel length was examined by numerical simulation (Chu et al., 2014) and field testing (Liu et al., 2019a). Subsequently, the difference in the unsteady slipstream between a single train and two trains was investigated numerically (Li et al., 2020). However, characteristic comparative analysis of aerodynamic pressure between a single train and two trains has not been carried out.

Therefore, we used the numerical method to explore the difference in the characteristics of aerodynamic pressure between a single train and two trains running in a double-track tunnel. First, we verified the accuracy of the numerical method by comparing the results from numerical simulation and on-site monitoring. Then, we explored the time-history curves of aerodynamic pressure. Finally, we looked at the difference in the characteristics of aerodynamic pressure associated with train–tunnel factors for a single train and two trains running in a double-track tunnel.

2 Methodology

2.1 Models

The prototype of the train model was a CRH380 train with eight units, and the tunnel model was a double-track tunnel with an area (S) of 100 m^2. These prototypes are commonly used in high-speed railway lines in China (Chu et al., 2014; Niu et al., 2017; Deng et al., 2020). For the train model (as shown in Fig. 1), the height and width were respectively 3.70 and 3.38 m, the lengths of the head and middle cars were respectively 26.5 and 25.0 m, and the total length of the car was 203.0 m. The streamlined length of the train nose was 12.0 m. In the tunnel model, the center distance of the double track was 5.0 m. The cross-sectional area of the train model was 11.22 m^2 and of the tunnel model was 100.00 m^2, and the corresponding blockage ratio (γ) was 0.1122. The train model was simplified as a smooth body to improve the computational efficiency of numerical simulation while ensuring computational accuracy (Chu et al., 2014; Li et al., 2019).

2.2 Model options

The overall layout and boundary conditions of the numerical model are shown in Figs. 2 and 3, respectively. The size of the simulation domain near the tunnel entrance was similar to that near the exit. The length, width, and height were respectively 600, 120, and 60 m, ensuring full development of the flow field in the domain (Chu et al., 2014; Lu et al., 2020; Du et al., 2022c). The overall numerical model was segmented into static zone 1 and dynamic zone 2. We used an interface boundary condition to implement the information exchange between zone 1 and zone 2. Sliding mesh technology was used to simulate the relative motion of the train in the tunnel (Li and Guan, 2012; Wang et al., 2018; Liu et al., 2020).

The interface allowed the exchange of information between sliding zone 2 and stationary zone 1. A sketch of the information exchange on the interface is shown in Fig. 4. When the sliding grid zone 2 slid to the left, the relative motion between zone 1 and zone 2 formed a common interface. The pressure information was transmitted between zones 2-I, 2-II, and 2-III and

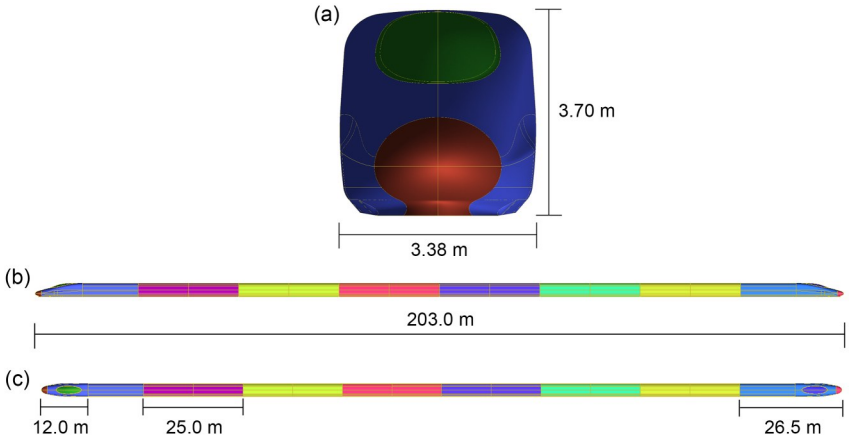

Fig. 1 Train model: (a) front view; (b) lateral view; (c) vertical view

zones 1-I, 1-II, and 1-III. The number of intersectional grids on the common interface changed when interface 2 of zone 2 slid relative to interface 1 of zone 1. The pressure information travelling through the common interface was calculated by the intersectional grids on the common interface. Thus, the information could be exchanged between adjacent zones.

Fig. 5 shows the time-history curves of aerodynamic pressure for different distances between the initial position of the train nose and the tunnel entrance. When the distance increased from 50.0 to 200.0 m, the differences in the maximum positive peak (MPP) and maximum negative peak (MNP) values were respectively 2.50% and 2.10%. Therefore, combining this information with the knowledge in the existing literature (Li and Guan, 2012; Lu et al., 2020), we set the distance as 50.0 m.

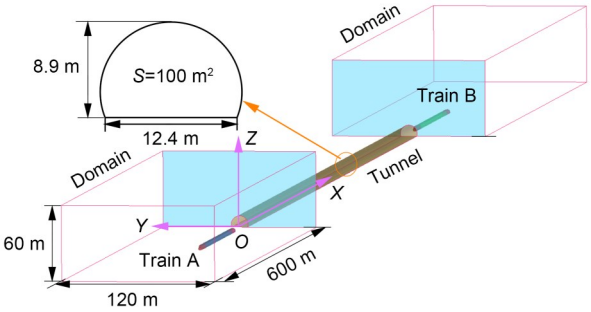

Fig. 2 Computational domain of the numerical model

2.3 Model mesh

Fig. 6 shows the mesh scheme adopted in the numerical model. The local meshes of the train nose and tunnel wall were refined to ensure computational accuracy. Mesh generation for the overall model was carried out using structured mesh technology (Liu et al., 2019a, 2020; Du et al., 2022a) to improve the meshing quality. The quality of the near-wall mesh could be evaluated by a non-dimensionless distance (y^+). The y^+ values of the train surface and the tunnel wall in our simulation were controlled between 30 and 180, which met the requirements of standard wall function (NRA, 2018). The minimum mesh sizes (h_0) of the train model and tunnel model were respectively 0.0075 and 0.0100 m, and the total number of meshes was 42.18 million.

We evaluated the influence of mesh density on the calculation results of numerical simulation. Three types of meshes, including fine (21.1 million cells), medium (15.5 million cells), and coarse (10.3 million cells), were selected. The train speed was set as 350 km/h,

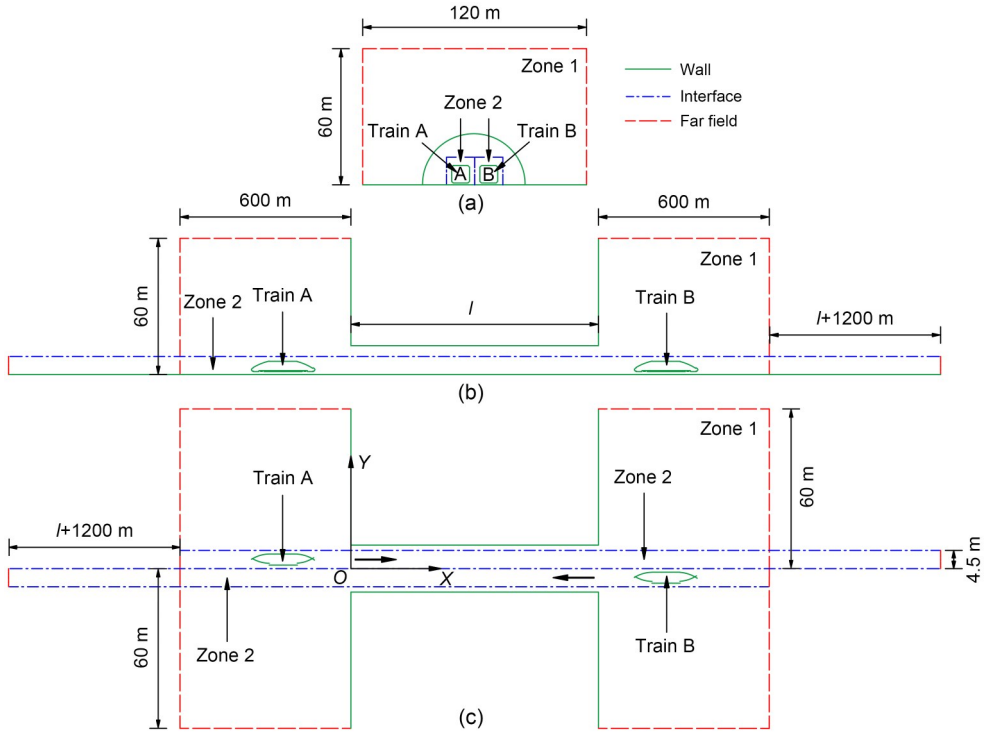

Fig. 3 Boundary conditions of the numerical model: (a) front view; (b) side view; (c) top view. *l* is the tunnel length

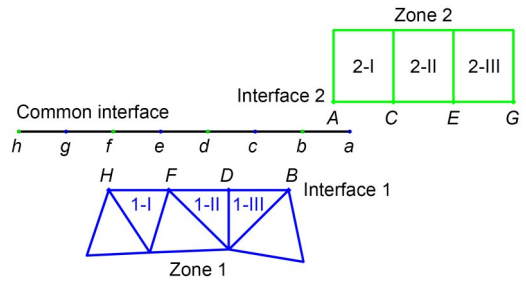

Fig. 4 Diagram of information exchange on the interface

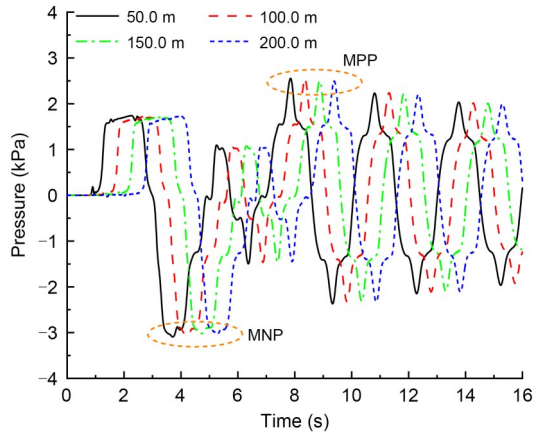

Fig. 5 Time-history curves of aerodynamic pressure for different distances between the initial position of the train nose and the tunnel entrance

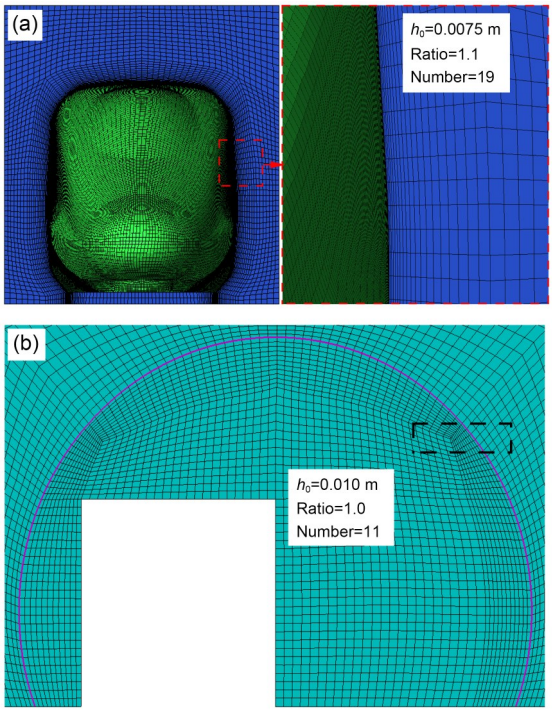

Fig. 6 Meshing scheme used in model: (a) train nose; (b) tunnel portal

and the tunnel length was 1000 m. The time-history curves of aerodynamic pressure for the three levels of mesh densities are shown in Fig. 7. The maximum peak-to-peak values of fine, medium, and coarse meshes were 3.362, 3.361, and 3.368 kPa, respectively. The difference between fine and medium meshes was smaller than that between fine and coarse meshes. Therefore, we used the medium mesh parameters in the subsequent numerical analysis.

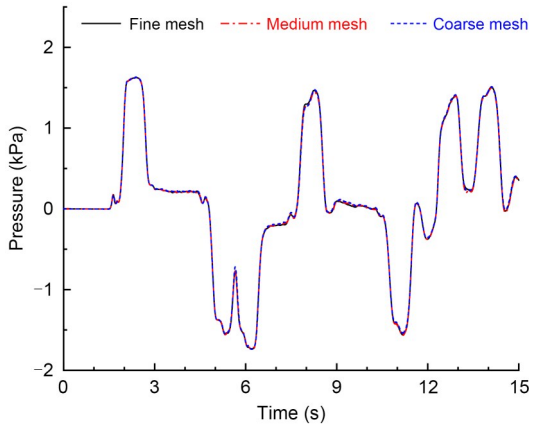

Fig. 7 Time-history curves of aerodynamic pressure for different mesh densities

2.4 Solver parameters

The renormalization group (RNG) k-ε two-equation turbulence model was used to simulate the turbulence characteristics of the flow field (Howe et al., 2008; Li et al., 2011). A finite volume-based fluid calculation software program was used to calculate the pressure and velocity. The coupling between the pressure field and velocity field was dealt with using the semi-implicit method for pressure linked equations (SIMPLE) algorithm, and the pressure field update was handled using the iterative method. Meanwhile, the second-order implicit scheme was used for the non-stationary term. The time step for all numerical calculations was set as 0.001 s, and the maximum iteration was taken as 50.

2.5 Computed conditions

The primary train–tunnel factors in this study were the train speed (v), l, and γ. The computed conditions of the numerical simulation are shown in Table 1. The height between the monitoring point and the ground was set as 1.5 m, while the distance between the monitoring point and the tunnel entrance was represented by its X-axis value.

Table 1 Computed conditions of the numerical simulation

Condition	v (km/h)	l (m)	γ
1	275	1000	0.1100
2	300	1000	0.1100
3	325	1000	0.1100
4	350	1000	0.1100
5	350	800	0.1100
6	350	600	0.1100
7	350	400	0.1100
8	350	200	0.1100
9	350	1000	0.1210
10	350	1000	0.1320
11	350	1000	0.1430
12	350	1000	0.1540
13	375	1000	0.1100
14	400	1000	0.1100

3 Validation

To estimate the calculation parameters and simulation results of the numerical method, we compared the calculation results with the monitoring results obtained in the field. Monitoring in the field was performed on the high-speed railway line from Beijing to Shanghai, China (Chen et al., 2017; Liu et al., 2018). For actual double-track tunnel, the length and the cross-sectional area were 978.0 m and 100 m^2, respectively. The monitoring points for aerodynamic pressure acting on the tunnel wall were located at a height of 1.5 m from the ground. The train type was CRH380 (with eight units), and the train speed was 300 km/h. For the numerical method, the small features of the train (such as lights, handlebars, bogies, and roof pantographs) and tunnel models were not considered, because the influence of these features on aerodynamic pressure is negligible (Du et al., 2022c). The other geometric dimensions of the train and tunnel models were the same as those in the field.

The comparison of aerodynamic pressure results is shown in Fig. 8. There is agreement between the time-history curves of aerodynamic pressure obtained by the two methods. The differences in the maximum positive and negative peak values for these two methods were respectively 3.27% and 1.42% at a measuring point located 500 m away from the tunnel entrance, and respectively 1.44% and 1.57% at a measuring point located 860 m away. Therefore, the simulation results and calculation parameters of the numerical method

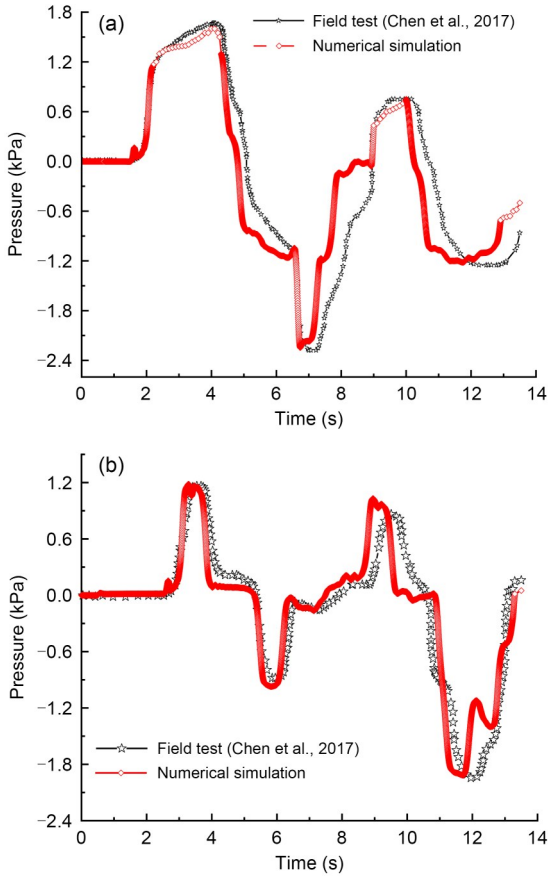

Fig. 8 Comparison of aerodynamic pressure between numerical and monitoring results: (a) monitoring point located 500 m away from the tunnel entrance; (b) monitoring point located 860 m away from the tunnel entrance

can be considered reasonable and reliable, and the calculation parameters can be employed in the subsequent analysis.

4 Results

4.1 Time-history curves of aerodynamic pressure

Fig. 9 shows the time-history curves of aerodynamic pressure in a tunnel's longitudinal middle section under different computed conditions. The aerodynamic pressure variation can be divided into stage I and stage II according to the change trend of the time-history curve, where stage I corresponds to irregular pressure fluctuations before the train tail leaves the tunnel exit, and stage II corresponds to periodic pressure decline after the train tail leaves the tunnel exit. The aerodynamic pressure simultaneously jumps positively or drops negatively in single-train and two-train

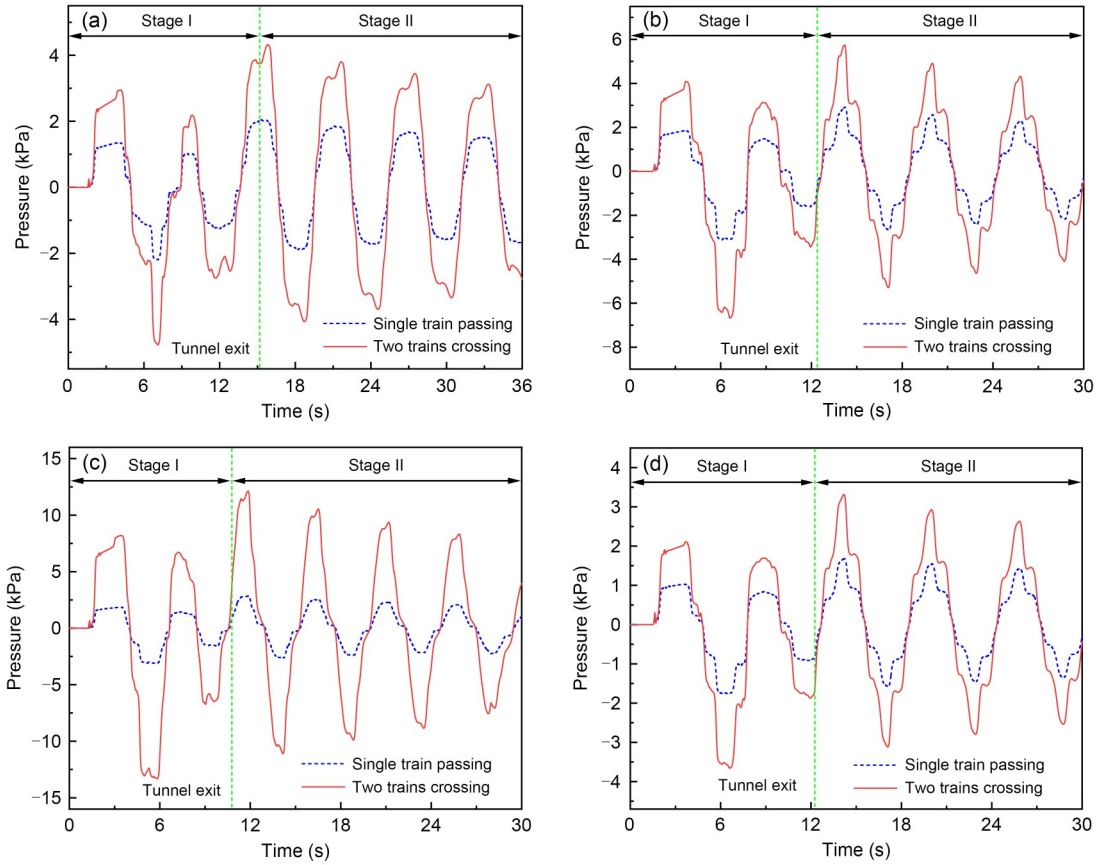

Fig. 9 Time-history curves of aerodynamic pressure in a tunnel's longitudinal middle section under different computed conditions: (a) computed condition 2; (b) computed condition 4; (c) computed condition 5; (d) computed condition 11

cases. The pressure amplitude of positive and negative peak pressures for the two-train case is larger than that for a single train.

Fig. 10 shows the relationship between the wave diagram in the tunnel and aerodynamic pressure variation in the tunnel's longitudinal middle section for computed condition 4 (v=350 km/h, l=1000 m, and γ=0.1100). The positive jump in aerodynamic pressure is induced by a compression wave and the train tail, for example, at the moments of t_1, t_4, t_5, t_7, and t_9. Similarly, the negative drop in aerodynamic pressure is induced by a rarefaction wave and the train nose, for example, at the moments of t_2, t_3, t_6, and t_8.

When two train noses enter the tunnel entrance, dual pressure waves are generated and both propagate forward toward the tunnel exit. Once dual pressure waves arrive at the tunnel exit, the corresponding reflected waves are generated and both propagate forward toward the tunnel entrance. The generation and reflection processes of the pressure waves caused by two trains leaving the tunnel exit are similar to those of two trains entering the tunnel entrance. Although the wave diagram for the two-train case is more complicated than that for the single-train case at the same speed, one interesting finding here is that the moments of pressure waves, and those of the train nose and tail arriving at the measuring section, such as the moments of t_1 to t_9, are coincident. The corresponding result is that the aerodynamic pressures jump or drop at the same time. The single pressure wave arrives at the measuring section when a single train is running in the tunnel, while two identical pressure waves arrive simultaneously when the two trains are running in the double-track tunnel. Accordingly, the amplitude of positive and negative peak pressures for the two-train case is higher than that for the single-train case.

Table 2 shows the maximum peak pressures in the tunnel's longitudinal middle section for computed condition 4 (v=350 km/h, l=1000 m, and γ=0.1100). Compared to the single-train case, the peak pressures are significantly influenced by the superimposed effect of the two-train case. For example, the MPP pressures

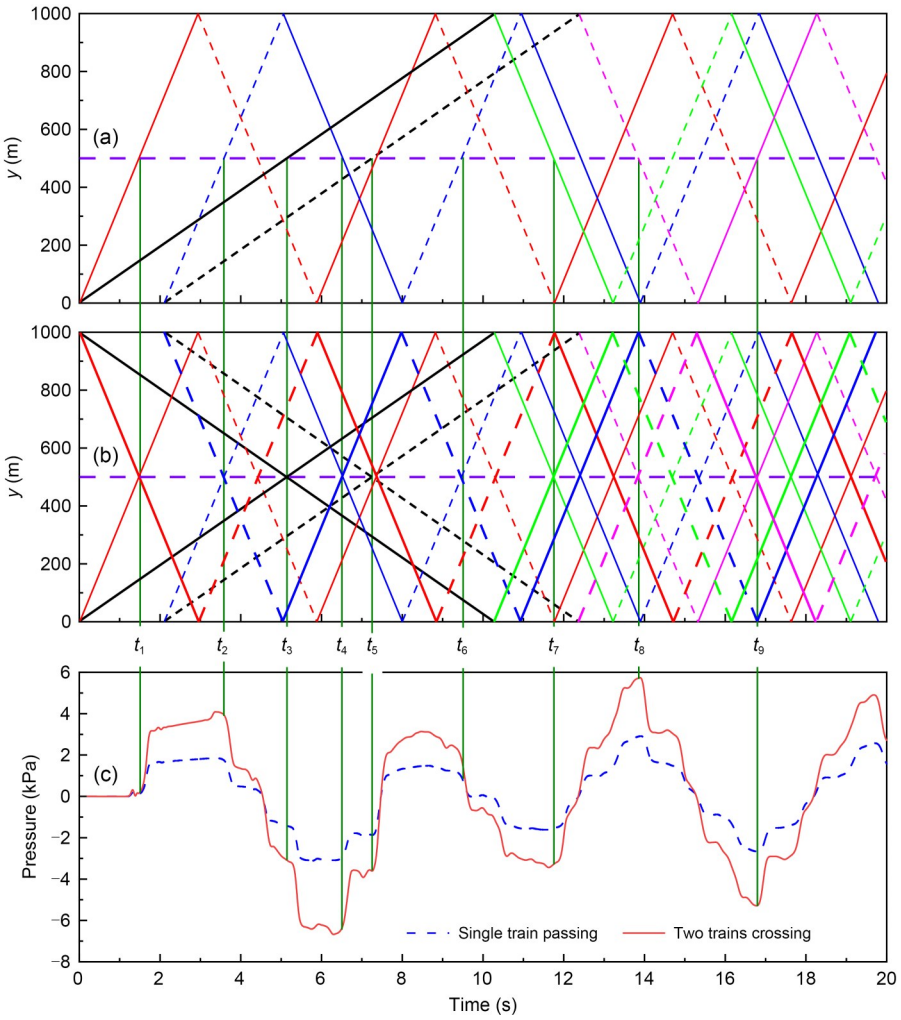

Fig. 10 Relationship between the wave diagram in the tunnel and pressure variation for computed condition 4: (a) wave diagram for single-train case; (b) wave diagram for two-train case; (c) pressure variation (x=500 m) for single-train and two-train cases. y indicates the distance from the tunnel entrance. The solid black lines indicate the travelling path of the train nose. Dotted black lines indicate the travelling path of the train tail. Red lines represent pressure waves induced by the train nose at the tunnel entrance. Green lines represent pressure waves caused by the train nose at the tunnel exit. Except for black lines, the solid lines denote compression waves, and the dotted lines denote rarefaction waves. The thin and thick lines represent the travelling path and corresponding wave diagram of train A and train B, respectively. In addition, the vertical olive-green lines indicate the moments when the pressure waves, train nose, and train tail reached the measuring section. References to color refer to the online version of this figure

Table 2 Maximum peak pressures in the tunnel's longitudinal middle section for computed condition 4

Stage	Case	Pressure (kPa)			
		MPP	P_{STP}	MNP	P_{STN}
I	Single-train	1.84	2.25	−3.11	3.57
	Two-train	4.09		−6.68	
II	Single-train	2.91	2.83	−2.67	2.59
	Two-train	5.74		−5.26	

in the single-train and two-train cases for stage I are 1.84 and 4.09 kPa, respectively. The MPP pressure difference (P_{STP}) between the single-train and two-train cases is 2.25 kPa, which is about 1.22 times the MPP pressure for the single-train case. The P_{STP} in stage II between the two cases is 2.83 kPa, about 0.97 times the MPP pressure for the single-train case. Similarly, the MNP pressure differences (P_{STN}) between the two cases in stages I and II are 3.57 and 2.59 kPa, respectively. These are 1.15 times and 0.97 times the MNP pressure for the single-train case, respectively. Hence, the superimposed effect of two trains has a larger influence on peak pressures in stage I than in stage II.

4.2 Train speed effect

4.2.1 Aerodynamic pressure in stage I

Fig. 11 shows the MPP and MNP pressure distributions along the tunnel longitudinal axis at 275 and 375 km/h in stage I (l=1000 m and γ=0.1100). The MPP and MNP pressures of the monitoring points near the middle section of the tunnel are generally larger than those near the tunnel portals. The P_{STP} and P_{STN} near tunnel portals are negligible. The P_{STP} and P_{STN} gradually increase from a tunnel portal to the middle section, reaching the maximum value at the tunnel's middle section. The histograms of the MPP and MNP pressures in the tunnel's longitudinal middle section at different train speeds in stage I are shown in Fig. 12. The amplitude of the maximum peak pressure increases as train speed rises to the power from 2.202 to 2.328. The relationships between the P_{STP} and P_{STN} and v in stage I are shown in Fig. 13. Similarly, the P_{STP} and P_{STN} increase as train speed rises to the power from 2.256 to 2.930.

4.2.2 Aerodynamic pressure in stage II

Table 3 shows the MPP and MNP pressures in the tunnel's longitudinal middle section at different train speeds in stage II (l=1000 m and γ=0.1100). There is no approximate linear relationship between the amplitudes of MPP and MNP pressures or between the P_{STP} and P_{STN} and the power of train speed. The MPP and MNP pressures increase with increasing train speed between 275 and 350 km/h. When train speed increases from 350 to 400 km/h, the MPP and MNP pressures first decrease and then increase.

4.3 Tunnel length effect

Fig. 14 shows the MPP and MNP pressure distributions along the tunnel's longitudinal axis with tunnel lengths of 400 and 800 m in stage I (v=350 km/h and

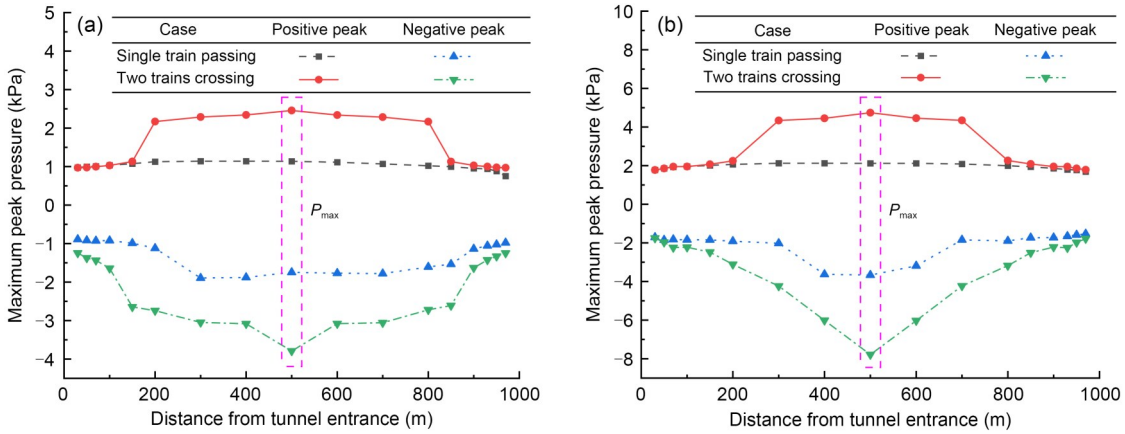

Fig. 11 Distributions of the maximum peak pressures along the tunnel longitudinal axis at train speeds of 275 and 375 km/h in stage I (l=1000 m and γ=0.1100): (a) v=275 km/h; (b) v=375 km/h

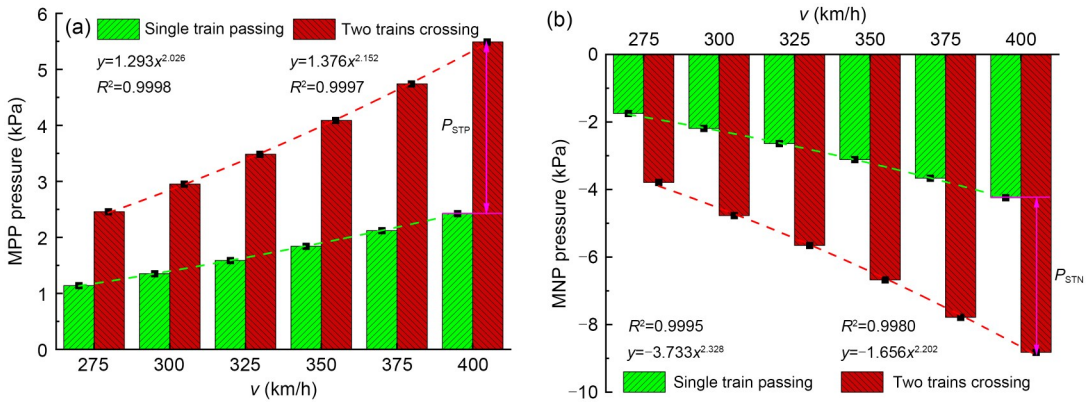

Fig. 12 Histogram of the maximum peak pressures in the tunnel's longitudinal middle section at different train speeds in stage I (l=1000 m and γ=0.1100): (a) MPP pressure; (b) MNP pressure

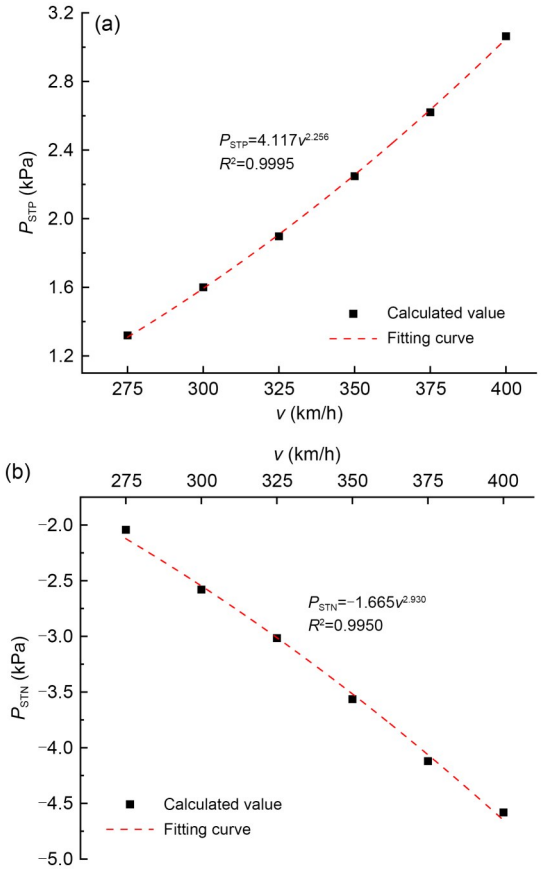

Fig. 13 Relationship between P_{STP} and P_{STN} and v in stage I (l=1000 m and γ=0.1100): (a) P_{STP}; (b) P_{STN}

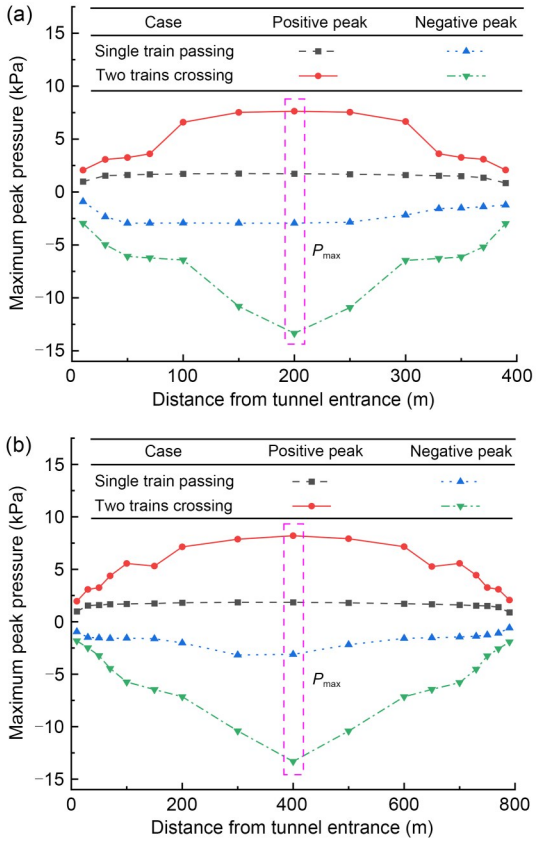

Fig. 14 Maximum peak pressure along the tunnel's longitudinal axis with tunnel lengths of 400 and 800 m in stage I (v=350 km/h and γ=0.1100): (a) l=400 m; (b) l=800 m

Table 3 Maximum peak pressures in the tunnel's longitudinal middle section at different train speeds in stage II (l=1000 m and γ=0.1100)

v (km/h)	Case	Pressure (kPa)			
		MPP	P_{STP}	MNP	P_{STN}
275	Single-train	1.40	1.45	−1.42	−1.62
	Two-train	2.85		−3.04	
300	Single-train	2.06	2.26	−1.89	−2.17
	Two-train	4.32		−4.06	
325	Single-train	2.52	2.46	−2.32	−2.35
	Two-train	4.98		−4.67	
350	Single-train	2.91	2.83	−2.68	−2.61
	Two-train	5.74		−5.29	
375	Single-train	1.71	2.22	−1.65	−2.01
	Two-train	3.93		−3.66	
400	Single-train	1.83	2.33	−1.55	−2.36
	Two-train	4.16		−3.91	

γ=0.1100). The influence of tunnel length on the distributions of the MPP and MNP pressures is similar to that of train speed, i.e., the MPP and MNP pressures and the P_{STP} and P_{STN} arrive at their maximum values at the tunnel's middle section. The histograms of MPP and MNP pressures in the tunnel's longitudinal middle section at different tunnel lengths in stages I and II are shown in Figs. 15 and 16, respectively. Compared with the single-train case, the MPP and MNP pressures increase significantly in the two-train case. Table 4 shows the P_{STP} and P_{STN} at different tunnel lengths in stages I and II. The MPP and MNP pressures of two trains, as well as the P_{STP} and P_{STN}, first increase and then decrease with the increase of tunnel length in stage I. There is a volatile relationship between the MPP and MNP pressures in the two-train case as well as the P_{STP} and P_{STN} and the tunnel length in stage II. However, the common phenomenon is that the MPP and MNP pressures in the two-train case and the P_{STP} and P_{STN} arrive at their maximum values when the tunnel length is between 600 and 800 m in stages I and II.

Based on the analysis above, we can conclude that when two trains are running in the double-track tunnel, the MPP and MNP pressures arrive at their maximum values when the tunnel length is between 600 and 800 m,

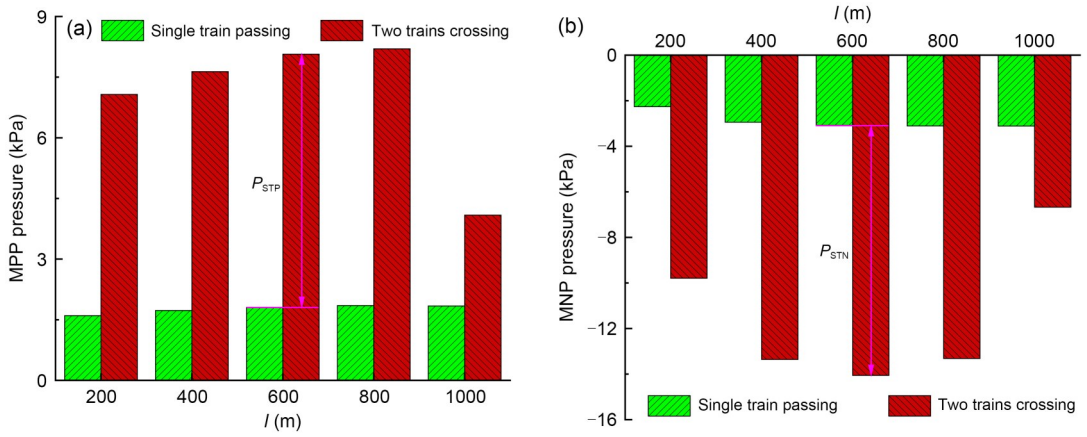

Fig. 15 Histogram of maximum peak pressure in the tunnel's longitudinal middle section with different tunnel lengths in stage I (v=350 km/h and γ=0.1100): (a) MPP pressure; (b) MNP pressure

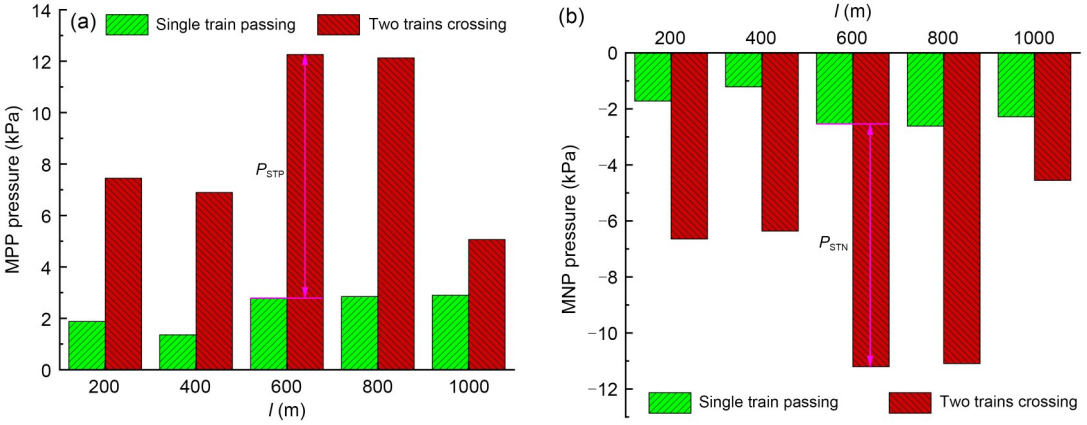

Fig. 16 Histogram of maximum peak pressure in the tunnel's longitudinal middle section with different tunnel lengths in stage II (v=350 km/h and γ=0.1100): (a) MPP pressure; (b) MNP pressure

Table 4 P_{STP} and P_{STN} in the longitudinal middle section with different tunnel lengths (v=350 km/h and γ=0.1100)

Stage	l (m)	Pressure (kPa)	
		P_{STP} (kPa)	P_{STN} (kPa)
I	200	5.47	−7.53
	400	5.91	−10.41
	600	6.26	−10.98
	800	6.35	−10.21
	1000	2.25	−3.56
II	200	5.57	−4.92
	400	5.54	−5.15
	600	9.48	−8.67
	800	9.28	−8.48
	1000	2.17	−2.27

which is quite close to the calculation result (710 m) of (CEN, 2006). The formula of the most unfavorable tunnel length ($l_{tu,crit}$) can be expressed as follows:

$$l_{\text{tu, crit}} = \frac{c}{2}\left(\frac{L_{\text{tr, 1}}}{v_{\text{tr, 1}}} + \frac{L_{\text{tr, 2}}}{v_{\text{tr, 2}}}\right), \tag{1}$$

where c is the sound speed; $L_{tr,1}$ and $L_{tr,2}$ are the lengths (203 m) of trains 1 and 2; $v_{tr,1}$ and $v_{tr,2}$ are the speeds (350 km/h) of trains 1 and 2, respectively.

4.4 Blockage ratio effect

Fig. 17 shows the MPP and MNP pressure distributions along the tunnel's longitudinal axis with blockage ratios of 0.0801 and 0.0863 in stage I (v= 350 km/h and l=1000 m). The influence of blockage ratio on the distributions of the MPP and MNP pressures is similar to that of train speed and tunnel length. The histograms of MPP and MNP pressures in the tunnel's longitudinal middle section with different blockage ratios in stages I and II are shown in Figs. 18 and 19, respectively. The variation law of aerodynamic

pressure with blockage ratio for the single-train case is similar to that for the two-train case. In stage I, the MPP and MNP pressures increase with the increase in the blockage ratio in both cases, and there is an approximately linear relationship between the P_{STP} and P_{STN} and the blockage ratio raised to the power from 2.186 to 2.527. In stage II, the MPP and MNP pressures increase with the increase in the blockage ratio

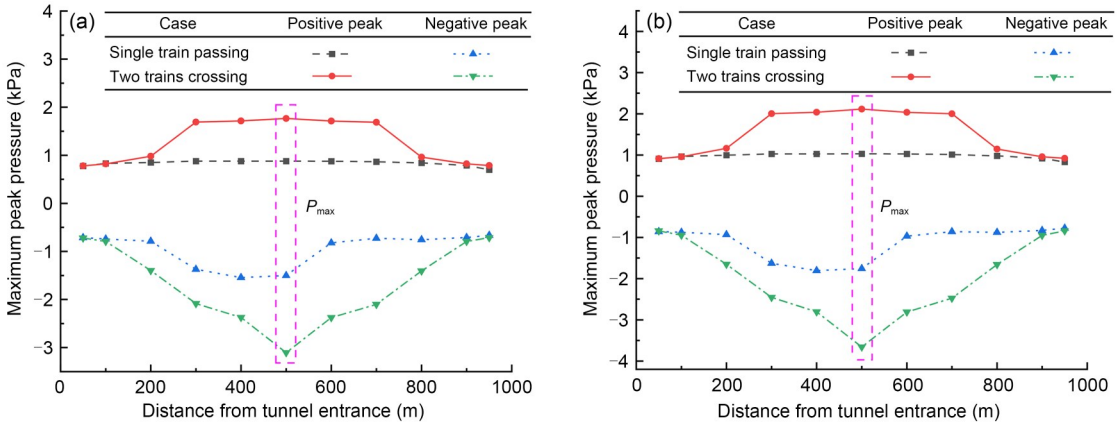

Fig. 17 Maximum peak pressure along the tunnel's longitudinal axis with blockage ratios of 0.0801 and 0.0863 in stage I (v=350 km/h and l=1000 m): (a) γ=0.0801; (b) γ=0.0863

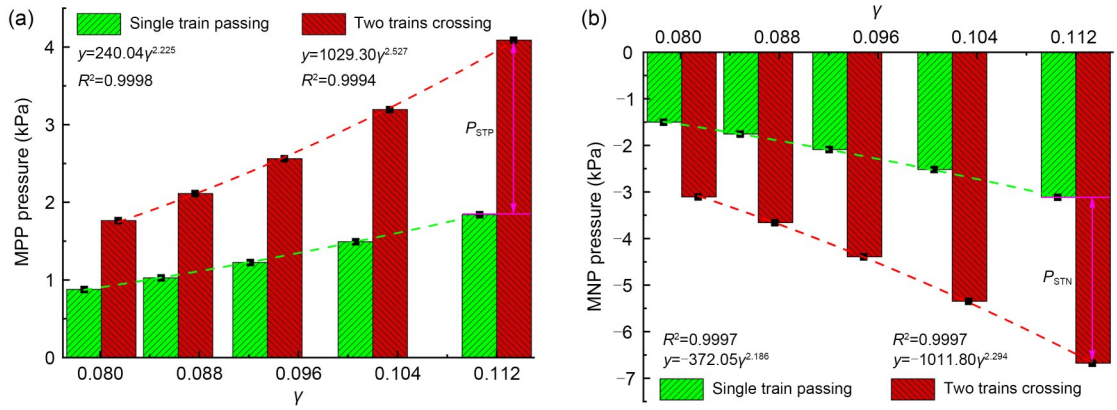

Fig. 18 Histogram of maximum peak pressure in the tunnel's longitudinal middle section with different blockage ratios in stage I (v=350 km/h and l=1000 m): (a) MPP pressure; (b) MNP pressure

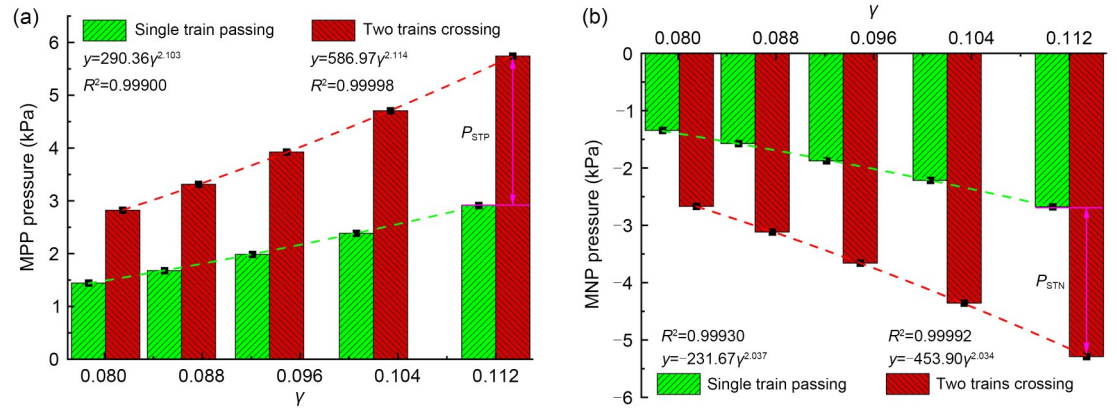

Fig. 19 Histogram of maximum peak pressure in the tunnel's longitudinal middle section with different blockage ratios in stage II (v=350 km/h and l=1000 m): (a) MPP pressure; (b) MNP pressure

for both cases, and there is an approximately linear relationship between the P_{STP} and P_{STN} and the blockage ratio raised to the power from 2.034 to 2.114. The relationships between the P_{STP} and P_{STN} and the blockage ratio in stages I and II are respectively shown in Figs. 20 and 21. Whether in stage I or stage II, the MPP and MNP pressures and the P_{STP} and P_{STN} increase with the blockage ratio. The amplitude of the MPP and MNP pressures, as well as the P_{STP} and P_{STN}, increase with the blockage ratio raised to the power from 2.032 to 2.798.

The relationships between MPP and MNP pressures, as well as the P_{STP} and P_{STN} in the tunnel's longitudinal middle section and influencing factors (v, l, and γ) in stages I and II, are shown in Table 5. P_i denotes the label of MPP pressure, MNP pressure,

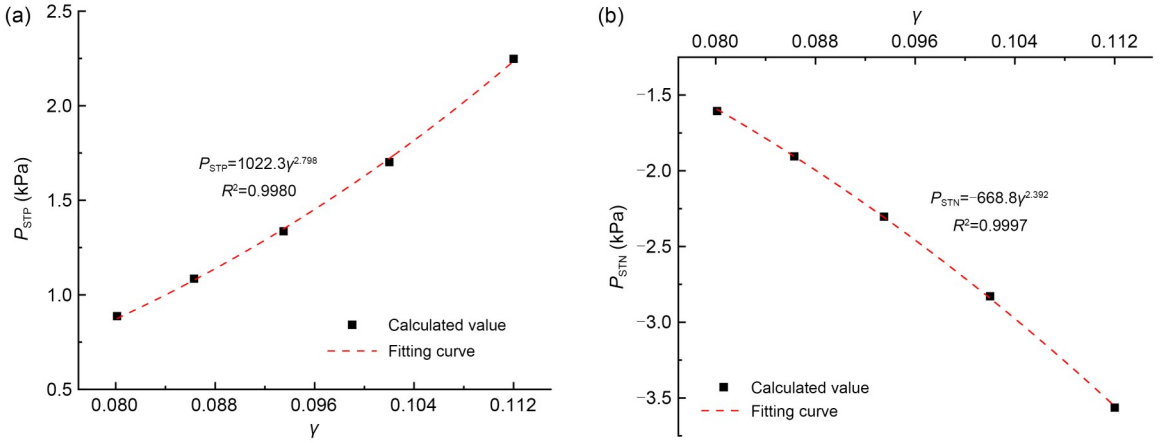

Fig. 20 Relationships between P_{STP} and P_{STN} and γ in stage I (v=350 km/h and l=1000 m): (a) P_{STP}; (b) P_{STN}

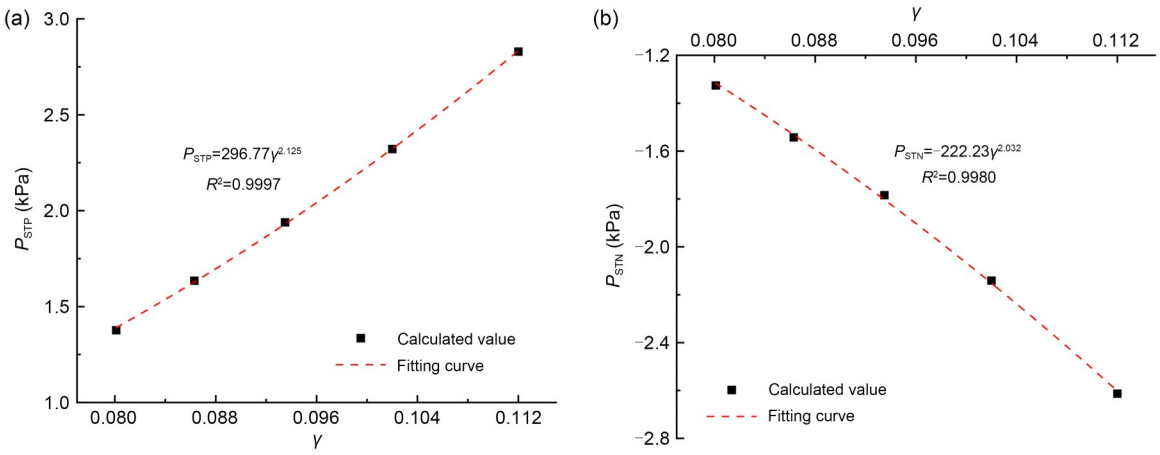

Fig. 21 Relationships between P_{STP} and P_{STN} and γ in stage II (v=350 km/h and l=1000 m): (a) P_{STP}; (b) P_{STN}

Table 5 Relationships between MPP and MNP pressures and P_{STP} and P_{STN} in the tunnel's longitudinal middle section and influencing factors (v, l, and γ)

Influencing factor	Value	Relationship	
		Stage I	Stage II
v (km/h)	275–350	$P_i=\alpha v^{\beta}$	P_i increases with increasing v
	350–400	$P_i=\alpha v^{\beta}$	P_i first decreases and then increases with increasing v
l (m)	200–1000	Stronger volatility between P_i and l	Stronger volatility between P_i and l
γ	0.0801–0.1122	$P_i=\zeta\gamma^{\delta}$	$P_i=\zeta\gamma^{\delta}$

P_{STP}, and P_{STN}. The labels α, β, ζ, and δ are the corresponding constants.

4.5 Engineering application

Affected by the aerodynamic pressure induced by high-speed trains travelling through a tunnel, microcracks in the tunnel lining continue to extend, expand, and interpenetrate, eventually leading to partial shedding. Shedding of the tunnel lining may affect the safe operation of high-speed trains in the tunnel.

Some analytical methods of examining the residual life of tunnel linings under aerodynamic pressure have been proposed (Liu et al., 2019b; Du et al., 2021). In this study, we looked at the influence of various factors of trains and tunnels on aerodynamic pressure. Therefore, the relationship between the residual life of tunnel lining and factors related to trains and tunnels can now be explored. After determining the model, marshalling form, and speed of a train, as well as the length and cross-sectional area of the tunnel, engineers should be able to predict the residual life of the lining of a high-speed railway tunnel.

5 Conclusions

The main conclusions that can be drawn from this study are:

(1) Aerodynamic pressure variation can be divided into stage I and stage II, according to the change trend of the time-history curve. Stage I corresponds to irregular pressure fluctuations before the train tail leaves the tunnel exit, and stage II corresponds to periodic pressure decline after the train tail leaves the tunnel exit. The aerodynamic pressures jump or drop simultaneously for both single-train and two-train cases. The pressure amplitude of the positive and negative peak values in the two-train case is larger than that in the single-train case.

(2) There is an approximately linear relationship between the P_{STP} and P_{STN} and train speed raised to the power from 2.256 to 2.930 in stage I. The P_{STP} and P_{STN} first decrease and then increase with the increase in train speed in stage II.

(3) The P_{STP} and P_{STN} first increase and then decrease with the increase in tunnel length in stage I. There is a volatile relationship between the P_{STP} and P_{STN} and tunnel length in stage II.

(4) In both stages I and II, the P_{STP} and P_{STN} increase with the blockage ratio. There is an approximately linear relationship between the P_{STP} and P_{STN} and the blockage ratio raised to the power from 2.032 to 2.798.

Acknowledgments

This work is supported by the Key Project of High-Speed Rail Joint Fund of National Natural Science Foundation of China (No. U1934210).

Author contributions

Jianming DU conducted the numerical calculation and wrote the first draft of the manuscript. Qian FANG revised the final version. Xuan ZHANG and Hualao WANG processed the data.

Conflict of interest

Jianming DU, Qian FANG, Xuan ZHANG, and Hualao WANG declare that they have no conflict of interest.

References

CEN (European Committee for Standardization), 2006. Railway Applications-Aerodynamics-Part 5: Requirements and Test Procedures for Aerodynamics in Tunnels, EN 14067-5: 2006. CEN.

Chen XD, Liu TH, Zhou XS, et al., 2017. Analysis of the aerodynamic effects of different nose lengths on two trains intersecting in a tunnel at 350 km/h. *Tunnelling and Underground Space Technology*, 66:77-90. https://doi.org/10.1016/j.tust.2017.04.004

Chen ZW, Liu TH, Zhou XS, et al., 2017. Impact of ambient wind on aerodynamic performance when two trains intersect inside a tunnel. *Journal of Wind Engineering and Industrial Aerodynamics*, 169:139-155. https://doi.org/10.1016/j.jweia.2017.07.018

Chu CR, Chien SY, Wang CY, et al., 2014. Numerical simulation of two trains intersecting in a tunnel. *Tunnelling and Underground Space Technology*, 42:161-174. https://doi.org/10.1016/j.tust.2014.02.013

Deng E, Yang WC, He XH, et al., 2020. Transient aerodynamic performance of high-speed trains when passing through an infrastructure consisting of tunnel–bridge–tunnel under crosswind. *Tunnelling and Underground Space Technology*, 102:103440. https://doi.org/10.1016/j.tust.2020.103440

Du J, Zhang L, Yang MZ, et al., 2020. Moving model experiments on transient pressure induced by a high-speed train passing through noise barrier. *Journal of Wind Engineering and Industrial Aerodynamics*, 204:104267. https://doi.org/10.1016/j.jweia.2020.104267

Du JM, Fang Q, Wang G, et al., 2021. Fatigue damage and residual life of secondary lining of high-speed railway tunnel under aerodynamic pressure wave. *Tunnelling and Underground Space Technology*, 111:103851. https://doi.org/10.1016/j.tust.2021.103851

Du JM, Fang Q, Wang G, et al., 2022a. Aerodynamic effects

produced by a high-speed train traveling through a tunnel considering different car numbers. *Symmetry*, 14(3):479. https://doi.org/10.3390/sym14030479

Du JM, Fang Q, Wang G, et al., 2022b. Analytical solution of a circular lined tunnel with alterable mechanical property under hydrostatic stress and internal pressure. *Journal of Central South University*, 29(8):2757-2770. https://doi.org/10.1007/s11771-022-5097-3

Du JM, Fang Q, Wang J, et al., 2022c. Influences of high-speed train speed on tunnel aerodynamic pressures. *Applied Sciences*, 12(1):303. https://doi.org/10.3390/app12010303

Gong C, Zhu ZD, 2018. Numerical study for the aerodynamic effects of high-speed trains on secondary lining. *Henan Science*, 36(5):721-727 (in Chinese). https://doi.org/10.3969/j.issn.1004-3918.2018.05.017

Howe MS, 2007. The genetically optimized tunnel-entrance hood. *Journal of Fluids and Structures*, 23(8):1231-1250. https://doi.org/10.1016/j.jfluidstructs.2007.06.005

Howe MS, Winslow A, Iida M, et al., 2008. Rapid calculation of the compression wave generated by a train entering a tunnel with a vented hood: short hoods. *Journal of Sound and Vibration*, 311(1-2):254-268. https://doi.org/10.1016/j.jsv.2007.09.012

Ko YY, Chen CH, Hoe IT, et al., 2012. Field measurements of aerodynamic pressures in tunnels induced by high speed trains. *Journal of Wind Engineering and Industrial Aerodynamics*, 100(1):19-29. https://doi.org/10.1016/j.jweia.2011.10.008

Li RX, Guan YJ, 2012. Investigation of air pressure pulse when two high-speed trains passing by each other in tunnel. *Journal of Mechanical Engineering*, 48(20):127-134 (in Chinese). https://doi.org/10.3901/JME.2012.20.127

Li WH, Liu TH, Huo XS, et al., 2019. Influence of the enlarged portal length on pressure waves in railway tunnels with cross-section expansion. *Journal of Wind Engineering and Industrial Aerodynamics*, 190:10-22. https://doi.org/10.1016/j.jweia.2019.03.031

Li WH, Liu TH, Chen ZW, et al., 2020. Comparative study on the unsteady slipstream induced by a single train and two trains passing each other in a tunnel. *Journal of Wind Engineering and Industrial Aerodynamics*, 198:104095. https://doi.org/10.1016/j.jweia.2020.104095

Li XH, Deng J, Chen DW, et al., 2011. Unsteady simulation for a high-speed train entering a tunnel. *Journal of Zhejiang University-SCIENCE A (Applied Physics & Engineering)*, 12(12):957-963. https://doi.org/10.1631/jzus.A11GT008

Liu F, Yao S, Zhang J, et al., 2018. Field measurements of aerodynamic pressures in high-speed railway tunnels. *Tunnelling and Underground Space Technology*, 72:97-106. https://doi.org/10.1016/j.tust.2017.11.018

Liu TH, Jiang ZH, Li WH, et al., 2019a. Differences in aerodynamic effects when trains with different marshalling forms and lengths enter a tunnel. *Tunnelling and Underground Space Technology*, 84:70-81. https://doi.org/10.1016/j.tust.2018.10.016

Liu TH, Jiang ZH, Chen XD, et al., 2019b. Wave effects in a realistic tunnel induced by the passage of high-speed trains. *Tunnelling and Underground Space Technology*, 86:224-235. https://doi.org/10.1016/j.tust.2019.01.023

Liu TH, Geng SG, Chen XD, et al., 2020. Numerical analysis on the dynamic airtightness of a railway vehicle passing through tunnels. *Tunnelling and Underground Space Technology*, 97:103286. https://doi.org/10.1016/j.tust.2020.103286

Lu YB, Wang TT, Yang MZ, et al., 2020. The influence of reduced cross-section on pressure transients from high-speed trains intersecting in a tunnel. *Journal of Wind Engineering and Industrial Aerodynamics*, 201:104161. https://doi.org/10.1016/j.jweia.2020.104161

NRA (National Railway Administration of the People's Republic of China), 2018. Railway Applications—Aerodynamics—Part 4: Requirements for Train Aerodynamic Simulation, TB/T 3503.4–2018. National Standards of the People's Republic of China (in Chinese).

Niu JQ, Zhou D, Liu TH, et al., 2017. Numerical simulation of aerodynamic performance of a couple multiple units high-speed train. *Vehicle System Dynamics*, 55(5):681-703. https://doi.org/10.1080/00423114.2016.1277769

Rivero JM, González-Martínez E, Rodríguez-Fernández M, 2018. Description of the flow equations around a high speed train inside a tunnel. *Journal of Wind Engineering and Industrial Aerodynamics*, 172:212-229. https://doi.org/10.1016/j.jweia.2017.09.012

Saito S, 2019. Optimizing cross-sectional area of tunnel entrance hood for high speed rail. *Journal of Wind Engineering and Industrial Aerodynamics*, 184:296-304. https://doi.org/10.1016/j.jweia.2018.11.028

Saito S, Fukuda T, 2020. Design of a tunnel entrance hood for high-speed trains. *Journal of Wind Engineering and Industrial Aerodynamics*, 206:104375. https://doi.org/10.1016/j.jweia.2020.104375

Wang TT, Wu F, Yang MZ, et al., 2018. Reduction of pressure transients of high-speed train passing through a tunnel by cross-section increase. *Journal of Wind Engineering and Industrial Aerodynamics*, 183:235-242. https://doi.org/10.1016/j.jweia.2018.11.001

Yang QS, Song JH, Yang GW, 2016. A moving model rig with a scale ratio of 1/8 for high speed train aerodynamics. *Journal of Wind Engineering and Industrial Aerodynamics*, 152:50-58. https://doi.org/10.1016/j.jweia.2016.03.002

Zhang L, Yang MZ, Liang XF, et al., 2017. Oblique tunnel portal effects on train and tunnel aerodynamics based on moving model tests. *Journal of Wind Engineering and Industrial Aerodynamics*, 167:128-139. https://doi.org/10.1016/j.jweia.2017.04.018